KeAi
CHINESE ROOTS
GLOBAL IMPACT

Available online at www.keaipublishing.com/en/journals/journal-of-magnesium-and-alloys/

ScienceDirect

Journal of Magnesium and Alloys 25 (2026) 102310

www.elsevier.com/locate/jma

Full Length Article

In situ EBSD characterization of static recrystallization in a Mg-Zn-Ca (ZX30) alloy

Abdulhamit Sarac[a,b,*], Tracy Berman[c], Varun S. Venkatesh[c], Ashwin J. Shahani[c,d], John Allison[a,c], Ashley Bucsek[a,c,*]

[a] *Department of Mechanical Engineering, University of Michigan, Ann Arbor, MI 48109, USA*
[b] *Department of Robotics and Autonomous Systems Engineering, Fatih Sultan Mehmet Vakif University, Istanbul, 34015, Turkiye*
[c] *Department of Materials Science and Engineering, University of Michigan, Ann Arbor, MI 48109, USA*
[d] *Chemical Engineering, University of Michigan, Ann Arbor, MI 48109, USA*

Received 5 June 2026; received in revised form 23 July 2026; accepted 23 August 2026

Abstract

The recrystallization behavior of a hot-compressed Mg–3Zn–0.1Ca (ZX30) alloy during static recrystallization was investigated *in situ* using electron backscatter diffraction (EBSD). The material was subjected to 5% plane-strain compression at 200 °C, and subsequently exposed to successive annealing treatments at 300 °C using a heating stage integrated with a scanning electron microscope (SEM)–EBSD system. The microstructural evolution and recrystallization process were monitored by performing EBSD scans immediately after each annealing step. Within this framework, three questions were addressed: (i) whether recrystallized grains can be reliably identified and quantified using EBSD metrics, (ii) whether recrystallized grains nucleate preferentially at grain boundaries, twin boundaries, or triple junctions, and (iii) whether grains with a Grain Orientation Spread (GOS) below 1° accurately represent the recrystallized fraction. Recrystallized grains were identified using grain-neighborhood, centroid, and orientation information through a graph-based approach. At the end of the process, the cumulative recrystallized grain area accounted for 28% of the total grain area. The analysis revealed that initially, approximately 70% of the recrystallized grains nucleated adjacent to twin boundaries, with this fraction gradually decreasing as the twin fraction decreased from an initial 15%. 36% of the recrystallized grains not adjacent to twin boundaries were initially observed to form at triple junctions. GOS maps indicated that many grains exhibited GOS values below 1° without undergoing recrystallization, exhibiting only recovery and growth. For the ZX30 alloy deformed to a low strain level (5%) at 200 °C, the present study reveals that the area fraction of grains with GOS below 1° could not be used as the sole metric for quantifying the recrystallized fraction. The total number of recrystallized grains as a function of the angle between the c-axis and the normal direction (ND) was determined, revealing a weakening of the basal texture for the annealed ZX30 alloy.

© 2026 Chongqing University. Publishing services provided by Elsevier B.V. on behalf of KeAi Communications Co. Ltd.
This is an open access article under the CC BY-NC-ND license (http://creativecommons.org/licenses/by-nc-nd/4.0/)

Keywords: Mg-Zn-Ca; *In situ* EBSD; Static recrystallization; GOS; KAM.

1. Introduction

The static recrystallization behavior of magnesium alloys has been extensively investigated to elucidate the mechanisms responsible for basal texture weakening, which results from annealing, and enhances the formability of these alloy systems. Basal texture weakening has been widely reported in magnesium alloys through the addition of rare-earth elements such as Er, Gd, Ce, La, and Nd, achieved via static recrystallization during annealing [1–11] or dynamic recrystallization [12–14]. More recently, calcium additions to magnesium–zinc alloys have been shown to induce basal texture weakening due to annealing or even texture randomization through static

Peer review under the responsibility of Chongqing University.
* Corresponding authors.
E-mail addresses: asarac@umich.edu (A. Sarac), abucsek@umich.edu (A. Bucsek).

https://doi.org/10.1016/j.jma.2026.102310
2213-9567/© 2026 Chongqing University. Publishing services provided by Elsevier B.V. on behalf of KeAi Communications Co. Ltd. This is an open access article under the CC BY-NC-ND license (http://creativecommons.org/licenses/by-nc-nd/4.0/)

recrystallization, offering a cost-effective alternative to rare-earth alloying [15–24].

Texture weakening during recrystallization of Mg–Zn–Ca alloys has been widely investigated. Kim et al. [16] reported texture weakening in rolled Mg–Zn–Ca sheet alloys after annealing, characterized by a splitting of the basal pole toward the transverse direction. Bohlen et al. [25] demonstrated that Ca addition to Mg–Zn alloys leads to texture weakening during static recrystallization upon annealing. Zeng et al. [17] further observed a weaker texture in fully recrystallized Mg–0.3Zn–0.1Ca compared with Mg–0.4Zn and Mg–0.1Ca alloys subjected to identical cold-rolling and annealing conditions. They hypothesized that the co-segregation of Zn and Ca to grain boundaries strongly influences grain boundary mobility by enhancing solute drag, an effect that was not observed for the Mg–Zn or Mg–Ca binary alloys. Luo et al. [18] showed that reducing the Zn and Ca contents in Mg–Zn–Ca alloys decreases the likelihood of second-phase formation, while increasing Ca content results in a reduction of peak texture intensity. Berman and Allison [19] reported that ternary Mg–Zn–Ca alloys exhibit significantly weakened basal textures during static recrystallization compared with unalloyed Mg and corresponding binary alloys, highlighting the importance of the combined effects of Zn and Ca additions.

Recrystallization in magnesium alloys can proceed through several mechanisms, including grain boundary nucleation, subgrain boundary migration, shear band nucleation, deformation twinning–assisted nucleation, and particle–stimulated nucleation [5,26]: (i) Grain boundary nucleation occurs along pre-existing grain boundaries where localized non-basal slip induces significant lattice rotations, facilitating the formation of new grains. (ii) Subgrain boundary migration involves the migration and coalescence of subgrain boundaries formed by self-organized dislocations during annealing, leading to the development of high-angle boundaries and recrystallized grains. (iii) Shear band nucleation arises within shear bands generated by intense plastic deformation, often associated with kink bands or twin-related shear processes, providing favorable sites for nucleation. Basu et al. [4] reported that recrystallization predominantly initiates within shear bands. Similarly, Zeng et al. [17] demonstrated that shear bands act as preferential nucleation sites in cold-rolled (with 23% and 40% thickness reduction) Mg–0.3Zn–0.1Ca alloys, while Guan et al. [27] also identified shear bands as favored nucleation regions during static recrystallization in Mg–rare–earth (Mg–RE) alloys. (iv) Deformation twinning–assisted nucleation is driven by the large lattice reorientations introduced by deformation twinning, with nucleation frequently observed at twin–twin intersections and twin–grain intersections. Basu and Al-Samman [28] demonstrated that, in Mg–RE alloys subjected to plane-strain compression (deformed to 6% and 13%), recrystallization preferentially nucleates at compression-twin and double-twin boundaries. Similarly, Shi et al. [29] reported that double twins serve as preferred nucleation zones during static recrystallization of uniaxially compressed Mg–3Al–1Zn alloys. Extending these observations, Ye et al. [30] showed that special CSL boundaries, such as Σ13a, exhibit preferential grain growth due to their higher mobility via grain boundary migration, whereas tension-twin boundaries are not favored nucleation sites despite the high density of tension twins in extruded unalloyed Mg. (v) In particle–stimulated nucleation, coarse second-phase particles promote recrystallization by generating local strain gradients and dislocation accumulation, whereas fine particles tend to inhibit boundary motion.

In the context of the mechanisms outlined above, the studies on Mg–Zn–Ca alloys reveal that solute effects and deformation substructures jointly govern recrystallization behavior. Luo et al. [18] proposed that recrystallization is governed primarily by two mechanisms: (i) Particle-stimulated nucleation associated with Ca segregation at grain boundaries [31], and (ii) a reduction in stacking fault energy and lattice size mismatch induced by Ca addition to the matrix [7,32]. Wang et al. [33] further demonstrated preferential grain growth of grains with specific orientations during static recrystallization of a low-alloyed, low-temperature extruded Mg–1.2Zn–0.1Ca alloy, which was attributed to the combined effects of stored strain energy and grain-boundary segregation leading to Zener pinning. More recently, Gomez et al. [34] demonstrated that in Mg–2Zn alloys, extension twinning and double twinning act as nucleation sites for recrystallized grains, whereas in Mg–0.5Ca alloys, contraction twinning and double twinning serve as the preferred nucleation sites. In contrast, extension twins in Mg–0.5Ca did not exhibit recrystallization. Despite these extensive studies on preferential nucleation sites and growth behavior during static recrystallization, a quantitative framework or metric capable of determining the fraction of recrystallized grains nucleating at twin boundaries or grain boundaries has not yet been reported.

The microstructural evolution during recrystallization in magnesium-aluminum and single-phase aluminum alloys has been extensively investigated using *in situ* electron backscatter diffraction (EBSD) [21,35–37]. The static recrystallization behavior of magnesium alloys containing rare-earth additions has primarily been examined using *in situ* [38] or *quasi in situ* EBSD [8–11,27,39,40]. In some *quasi in situ* EBSD studies, annealing is conducted in a furnace under an inert gas atmosphere, with the sample often sealed in aluminum foil and subsequently quenched; prior to each scan, surface oxides are removed by polishing using a suspension or by ion etching. Fiducial markers are introduced on the sample surface to enable repeated examination of the same area during successive EBSD scans. Only a limited number of *quasi in situ* EBSD studies have addressed static recrystallization in Mg–Zn binary and Mg–Zn–Ca ternary alloys [17,41]. More recently, *in situ* EBSD has been applied to study static recrystallization in unalloyed magnesium [30] and Mg–(Zn, Ca) binary alloys [34], while *in situ* far-field high-energy X-ray diffraction microscopy (HEDM) has been employed to investigate static recrystallization in hot-compressed Mg–Zn–Ca alloys [20,24]. To the best of our knowledge, the present work is the first to employ *in situ* EBSD for direct tracking of the recrystallized grains, static recrystallization kinetics, microstructural evolution, and texture development in hot-compressed Mg–

Zn–Ca alloys. This approach establishes a quantitative framework for characterizing static recrystallization by enabling the direct observation of individual recrystallized grains, the spatial distribution of recrystallized grains adjacent to grain boundaries, twin boundaries, and triple junctions, and the texture weakening during annealing. In particular, the progressive weakening of the basal texture contributes to improved formability of magnesium alloys. Therefore, the findings provide quantitative insights that can assist in optimizing thermomechanical processing parameters to tailor the microstructure, texture, and consequently the formability of Mg–Zn–Ca alloys.

A threshold for grain orientation spread (GOS) less than or equal to 1° is widely used as a conventional criterion for identifying recrystallized grains [11,19,21,22,24,25,42–46]. Accordingly, the recrystallized area fraction is commonly calculated as the ratio of the total area of grains with GOS $\leq$ 1° to the total grain area. In this study, we aim to examine whether non-recrystallized grains may also exhibit GOS values $\leq$ 1°, thereby evaluating the reliability of this commonly used criterion for identifying recrystallized grains. To this end, we employ a graph-based approach that enables robust identification of recrystallized grains [47]. This approach provides a direct framework for comparing the GOS values of recrystallized and non-recrystallized grains throughout the annealing process.

Despite the considerable progress made in understanding the static recrystallization behavior of magnesium alloys, several fundamental scientific questions concerning the quantitative characterization of static recrystallization remain unresolved. Can recrystallized grains be reliably identified and quantified using EBSD-based metrics? Where do recrystallized grains preferentially nucleate during static recrystallization adjacent to the grain boundaries, twin boundaries, or at triple junctions? Does the conventionally used Grain Orientation Spread (GOS) criterion of $\leq$1° accurately represent the recrystallized fraction?

To address these questions, the static recrystallization behavior of a hot-compressed Mg–Zn–Ca alloy was characterized at 300 °C by successive annealing using *in situ* EBSD. Recrystallized grains were then identified and quantified using a graph-based approach, enabling direct grain tracking throughout the annealing process. The evolution of recrystallization was systematically analyzed. Grain boundaries were quantitatively assessed as potential nucleation sites by evaluating the number of neighboring grains surrounding recrystallized grains, while the fraction of newly recrystallized grains nucleating at twin boundaries was also quantified, providing insight into preferential nucleation locations. In addition, the robustness of the conventional Grain Orientation Spread (GOS) threshold method for determining recrystallized grain fractions was critically assessed. The feasibility of employing a Kernel Average Misorientation (KAM)-based threshold for recrystallized grain identification was also examined. Finally, texture evolution was analyzed to elucidate basal texture weakening and progressive texture randomization during static recrystallization.

2. Experimental procedure

Rectangular parallelepiped specimens (20 mm × 15 mm × 10 mm) were machined from 30 mm diameter extruded rods of Mg-3wt%Zn-0.1wt%Ca (ZX30) solution treated at 325 °C for 1 h. The extrusions were provided by Canmet Materials. Plane strain compression (PSC) tests were conducted using a Gleeble 3500 thermomechanical processing simulator, as illustrated in Fig. 1(a), with the normal direction (ND) aligned parallel to the compression axis (and the prior extrusion direction) and the rolling direction (RD) oriented perpendicular to the compression axis. The Gleeble system employs direct resistance heating, controlled via feedback from a thermocouple spot-welded to the specimen surface. After heating the specimens to 200 °C, the specimens were deformed to a compressive strain of 5% at a strain rate of 0.5 s^{-1}. After deformation, the specimens were rapidly cooled by forced air quenching. The true stress–strain response obtained during plane strain compression is shown in Fig. 1(b).

The deformation and annealing conditions used in this study were selected based on previous investigations of static recrystallization in Mg–Zn–Ca alloys [19,20,48], particularly the work of Montiel et al. [48]. In that study, recrystallization was examined after 5, 10, and 20% plastic deformation followed by annealing at temperatures between 275 °C and 350 °C. The time required to reach 50% recrystallization, as measured using the grain orientation spread (GOS) technique, was 4 min or less under the conditions examined, indicating that recrystallization proceeds rapidly in this alloy system. Therefore, in the present work, a relatively low deformation level of 5% and an annealing temperature of 300 °C were selected to promote static recrystallization on a timescale suitable for *in situ* EBSD characterization. These conditions enabled nucleation, grain growth, and the evolution of individual recrystallized grains to be tracked at multiple time points during the early and intermediate stages of recrystallization. The influence of higher deformation levels on static recrystallization in Mg–Zn–Ca alloys will be examined in future work.

For *in situ* heating and *in situ* EBSD characterization, smaller specimens measuring 3 mm × 4 mm with a thickness of 2 mm were extracted from the center of the PSC-deformed specimens using electrical discharge machining (EDM). The surface intended for EBSD analysis (3 mm × 4 mm) was subsequently prepared by mechanical grinding and polishing under low applied forces to minimize the introduction of deformation-induced artifacts, followed by chemical etching in a solution of 10 mL water, 10 mL acetic acid, 4.3 g of picric acid crystals, and 70 mL of ethanol for 5 s.

Following surface preparation, the side opposite to the polished surface was mounted onto a copper sample holder using a conductive adhesive to ensure both mechanical stability and efficient thermal and electrical contact during heating and scanning. The sample holder was then installed onto a NewTec MT1000 heating stage as shown in Fig. 2(a). The MT1000 heating stage consists of a dual-disc furnace configuration, with temperature control provided by two embedded

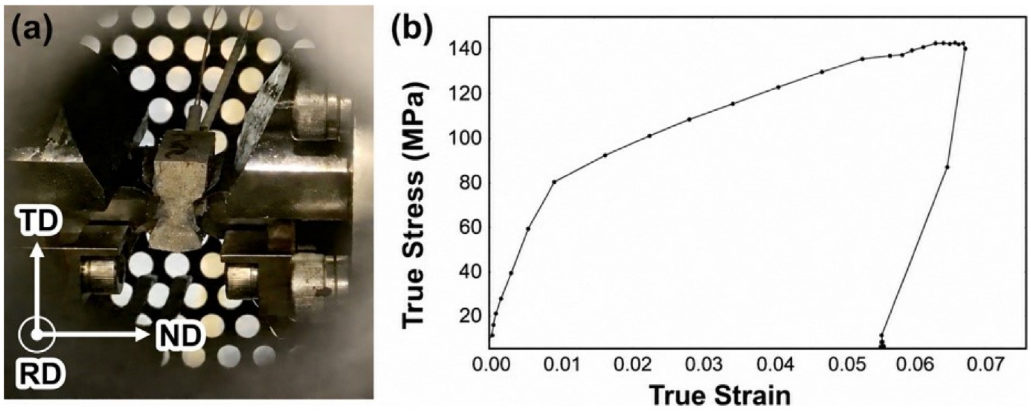


Fig. 1. Deformation of rectangular parallelepiped specimens: (a) Plane strain compression tests conducted using a Gleeble 3500 thermomechanical simulator; (b) compressive true stress as a function of compressive true strain.

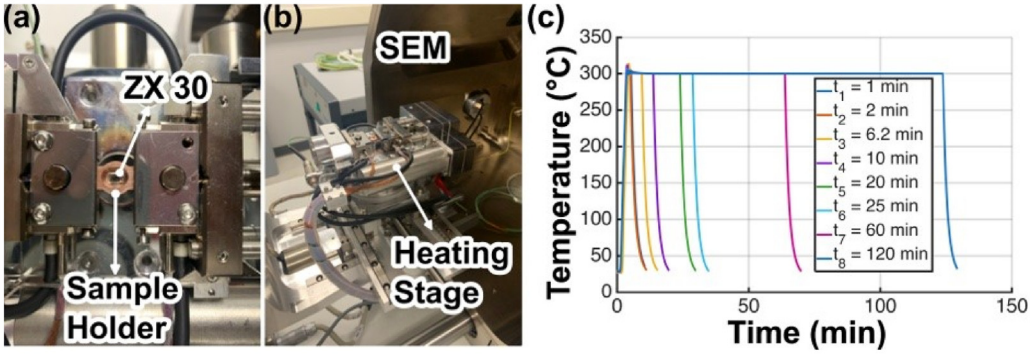


Fig. 2. Specimen mounting, heating stage, and SEM configuration for annealing and *in situ* EBSD: (a) Mg–Zn–Ca specimen (ZX30) attachment to the copper sample holder and heating stage; (b) NewTec MT1000 heating stage mounted on the Tescan MIRA3 SEM stage; (c) annealing process showing temperature as a function of time.

thermocouples and an additional spring-loaded thermocouple in direct contact with the underside of the specimen to enable accurate temperature monitoring at the sample location.

The heating stage was mounted inside a Tescan MIRA3 scanning electron microscope (SEM) equipped with an EDAX Hikari EBSD system, as shown in Fig. 2(b). All annealing steps were performed with a constant heating ramp rate of 2 °C/s to a target temperature of 300 °C as shown in Fig. 2(c). After each annealing step, the specimen was cooled by introducing nitrogen (N_2) gas into the SEM vacuum chamber to rapidly reduce the temperature and preserve the microstructure prior to characterization. After cooling to room temperature, EBSD scans were acquired over a 500 μm × 500 μm area using a step size of 0.33 μm. The annealing and *in situ* EBSD characterization procedure was conducted in a stepwise manner, with individual annealing holds of 1, 2, 6.2, 10, 20, 25, 60, and 120 min at 300 °C. The total duration of all *in situ* annealing steps is 244.2 min. A final *ex situ* annealing step of 240 min at 300 °C was performed in a Thermolyne box furnace, resulting in a final total annealing time of 484.2 min.

Owing to the manual determination of the scan center for each measurement, slight shifts in the spatial positioning of grains are evident between successive datasets. To enable a direct comparison of the IPF-Z maps across consecutive annealing steps, a post-processing procedure was applied wherein the maps were cropped and resized to ensure consistent fields of view.

The workflow used to correct spatial shifts between successive measurements is shown in Fig. 3(a–d). The initial, unheated condition at $t = 0$ min, as shown in Fig. 3(a), was selected as the reference state. The spatial bounds of the reference map were determined, and a subset of grains within this region was selected as seed grains. These grains were then matched to the same grains in the next annealing step for $t = 1$ min as shown in Fig. 3(b) based on orientation, centroid position and neighborhood topology. This approach is described in further detail by Venkatesh et al. [47]. The centroids of these matched grains were then used to compute the average translational shift between consecutive time steps as shown in Fig. 3(c). This average shift was used to calculate the cumulative displacement relative to the reference frame, and the common inner bounding region shared by all images across the time steps was iteratively updated, as shown in Fig. 3(b), where the edges of the bounding region are indicated by dashed lines. Finally, the initial map was cropped according to the bounding region to obtain the aligned EBSD map as shown in Fig. 3(d). This procedure was repeated for each time step, yielding spatially aligned

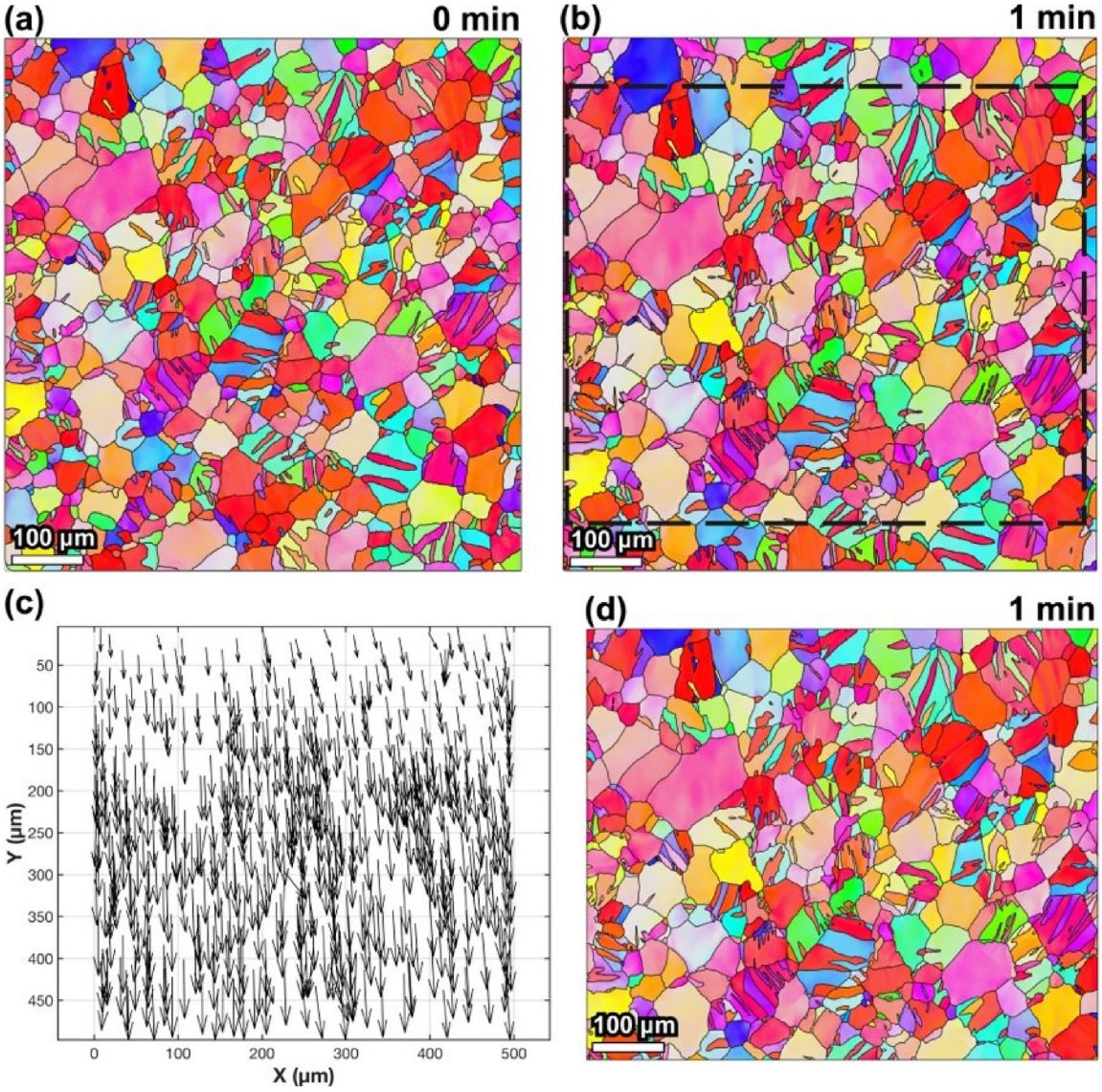


Fig. 3. Post-processing procedure applied to compensate for spatial shifts between successive EBSD maps, where Z denotes the out-of-plane normal direction: (a) IPF-Z map of the reference frame at $t = 0$ min (unheated); (b) IPF-Z at $t = 1$ min, where the edges of the bounding region are indicated by dashed lines, defining the area of overlap with the reference frame; (c) displacement vectors representing the relative shifts of grain centroids between $t = 0$ min and $t = 1$ min; (d) final cropped IPF-Z map at $t = 1$ min after alignment with the reference frame.

IPF-Z maps suitable for direct comparison. After applying the shift-correction procedure, the EBSD maps presented as IPF-Z color maps are shown in Fig. 4(a–i). All subsequent quantitative analyses and comparisons throughout this study are based on these corrected datasets.

3. Results

3.1. Microstructure evolution

Inverse pole figure (IPF) maps along the normal direction (IPF-Z) were obtained for the initial, unheated condition and for the eight subsequent annealing steps, as shown in Fig. 4(a–i). Immediate observations from these maps are the progressive depletion of twinned grains during annealing, the decrease in the number of grains overall, and the systematic increase in grain size.

The number of grains was 500 in the initial, unheated condition ($t = 0$ min). As shown in Fig. 5(a), the grain count begins to decrease notably after an annealing duration of 9.2 min, reaching approximately 160 by the end of annealing. Correspondingly, the average grain diameter was initially 20 µm and exhibits a rapid increase beyond 9.2 min of annealing, with a value of approximately 40 µm at the final annealing stage, as illustrated in Fig. 5(b). The evolution of the twin fraction is presented in Fig. 5(c). The initial twin fraction was approximately 15%, decreasing to about 10% after 9.2 min of annealing. With continued annealing, the fraction of twinned regions progressively diminishes, with twins becoming nearly absent at the end of annealing.

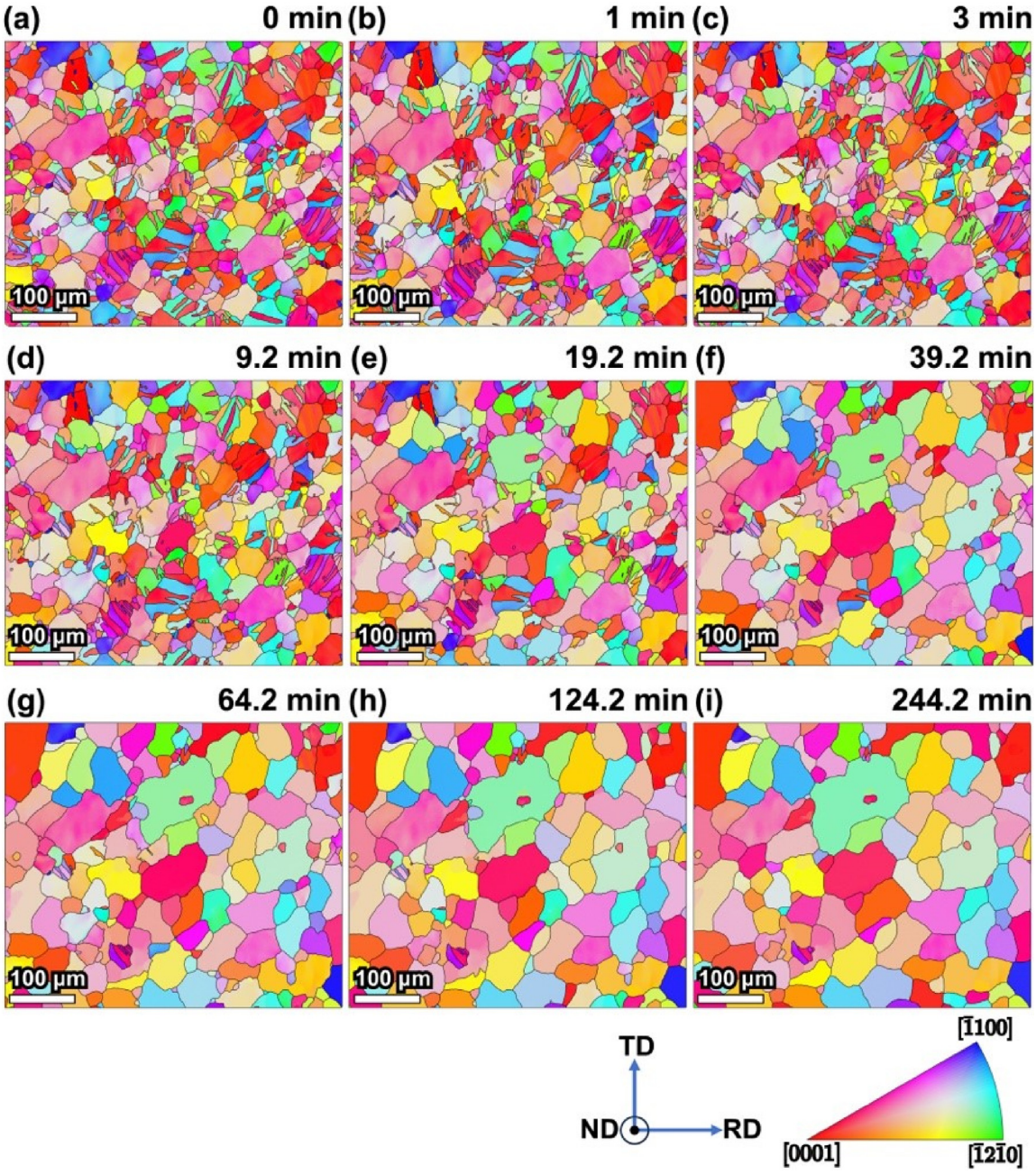


Fig. 4. Shift-corrected *in situ* inverse pole figure (IPF-Z) maps along the normal direction for the initial condition and successive stepwise annealing treatments at 300 °C: (a) $t = 0$ min without heating; (b) $t = 1$ min; (c) $t = 3$ min; (d) $t = 9.2$ min; (e) $t = 19.2$ min; (f) $t = 39.2$ min; (g) $t = 64.2$ min; (h) $t = 124.2$ min; (i) $t = 244.2$ min.

3.2. Individual grain trajectories

The trajectories of individual grains were examined at five representative annealing steps, including the initial unheated condition ($t = 0$ min) and subsequent annealing times of $t = 3$, $t = 19.2$, $t = 39.2$, and $t = 244.2$ min, which were selected as illustrative cases as shown in Fig. 6(a–e). Based on their morphological evolution and stability during annealing, six representative grains were selected. Grain A remained nearly unchanged throughout the annealing process, indicating a high degree of morphological stability. Grain B corresponds to a recrystallized grain that exhibited gradual growth while persisting throughout the entire annealing sequence. Grain C represents a twinned grain that underwent pronounced growth during annealing.

Grain D is a non-recrystallized grain that increased in size over time. Grain E corresponds to a highly twinned grain that progressively shrank during annealing and was nearly eliminated at the final annealing stage. Finally, Grain F is another recrystallized grain that nucleated at a twin boundary and subsequently grew gradually with continued annealing.

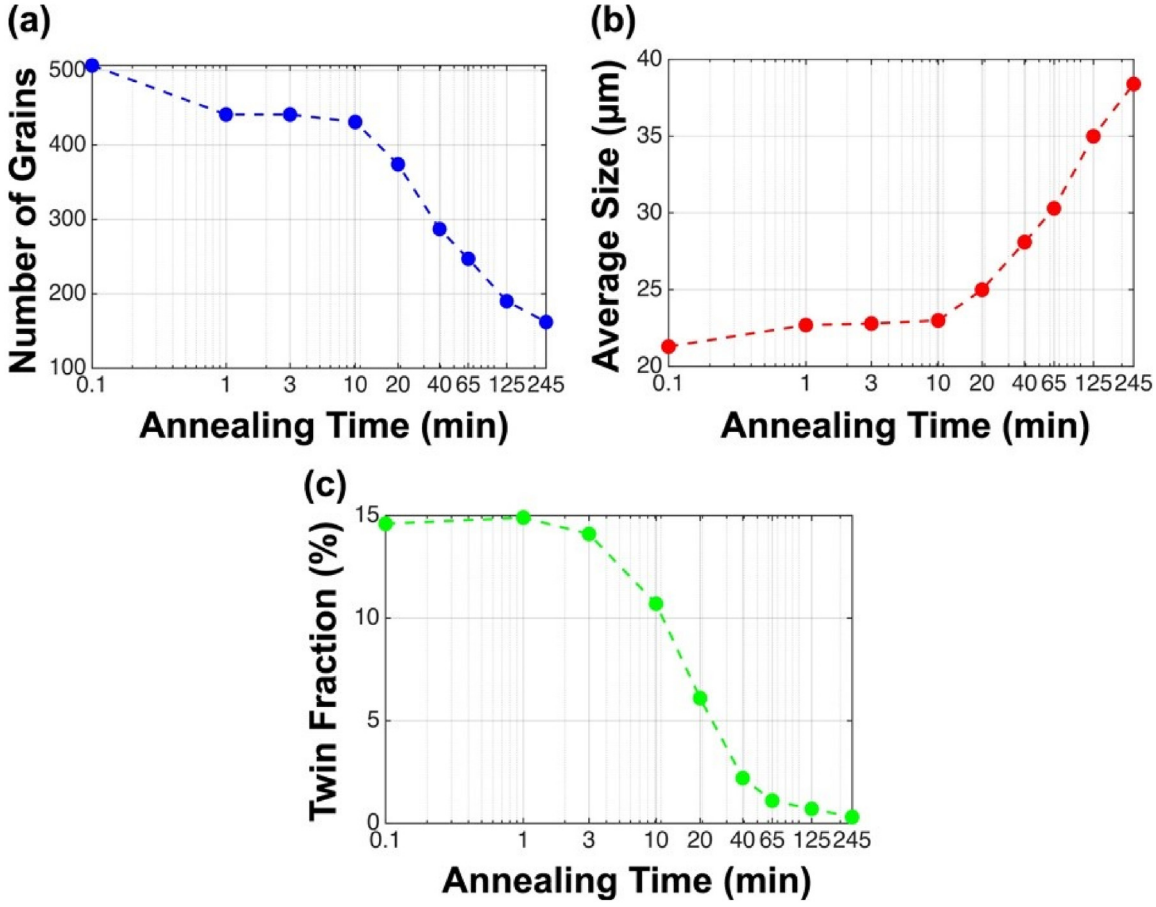


Fig. 5. Evolution of the microstructure during the annealing process. The annealing time is presented on a logarithmic scale in all plots: (a) number of grains as a function of annealing time; (b) average grain diameter as a function of annealing time; (c) twin fraction (%) as a function of annealing time.

3.3. Identification and quantification of recrystallized grains

Recrystallized and non-recrystallized grains were identified by tracking grains using graph–based approach [47], which relies on three key elements associated with each grain: (i) the adjacency list defining the local neighborhood topology, (ii) the centroid positions of the neighboring grains, and (iii) the crystallographic orientations of the grains. These elements were extracted for each annealing step, as schematically illustrated in Fig. 7(a,b). Based on this information, a graph-based tracking scheme was implemented to compare grain neighborhoods between two successive annealing steps. Recrystallized grains were defined as grains that could not be reliably matched to any grain in the preceding annealing step using neighborhood topology, centroid proximity, and crystallographic orientation.

In Fig. 8, the entire grain map before annealing is shown in Fig. 8(a), and only the recrystallized grains at successive annealing steps are presented in Fig. 8(b–i). Newly recrystallized grains (i.e., recrystallized grains that appear for the first time at a particular annealing step) are outlined in thick black lines, and recrystallized grains that appeared at some earlier time steps are not outlined. For example, the recrystallized grain indicated by the pink arrow was first identified at $t = 1$ min (Fig. 8(b)), remained present through $t = 19.2$ min (Fig. 8(e)), and was no longer visible on the examined surface by $t = 39.2$ min (Fig. 8(f)). The yellow arrow points to a recrystallized grain that first detected at $t = 3$ min as shown in Fig. 8(c), which continued to coarsen through the final annealing stage. The red arrow indicates another recrystallized grain, also identified in Fig. 8(b), that continued to grow throughout the annealing process.

The evolution of the number of new recrystallized grains versus the total number of recrystallized grains is shown in Fig. 9(a). Approximately 40 recrystallized grains remain at the final stage of the annealing process (out of roughly 160 total grains). The number of new recrystallized grains decreases with annealing time and becomes negligible beyond the annealing step at $t = 64.2$ min. The area fraction associated with the total recrystallized grains is illustrated in Fig. 9(b). By the end of the annealing sequence, the cumulative area fraction of recrystallized grains accounts for approximately 28% of the total grain area.

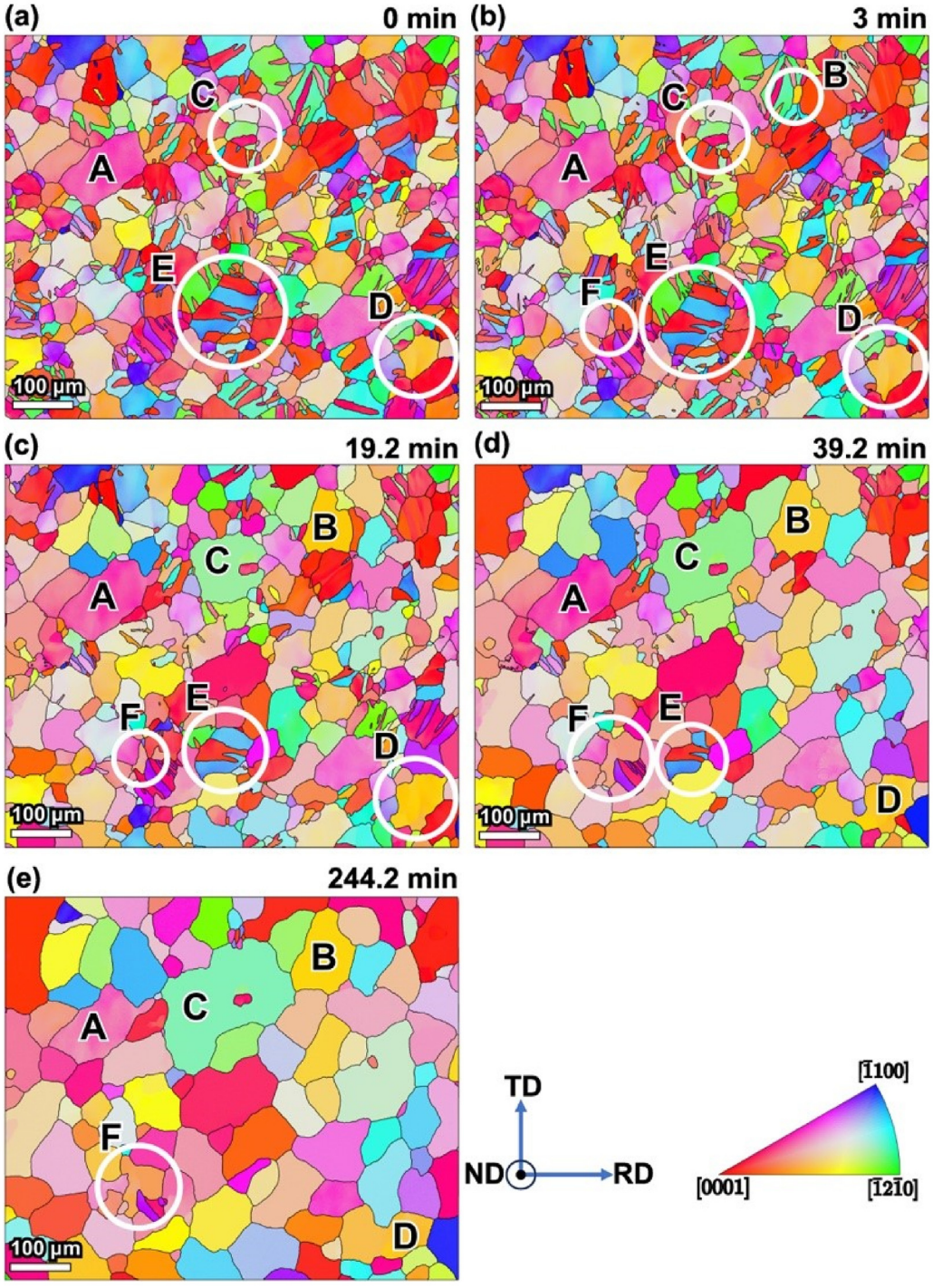


Fig. 6. The trajectories of individual grains at five representative annealing steps: (a) t = 1 min; (b) t = 3 min; (c) t = 19.2 min; (d) t = 39.2 min; (e) t = 244.2 min. To track the evolution of the grains, selected grains are highlighted with circles and labeled A–F.

4. Discussion

4.1. Recrystallization kinetics

The static recrystallization kinetics of the Mg–Zn–Ca alloy was analyzed using the Johnson–Mehl–Avrami–Kolmogorov (JMAK) relationship, based on the evolution of the recrystallized fraction as a function of annealing time. The recrystallized area fraction, $X(t)$, can be expressed as:

$$X(t) = 1 - \exp\left[-0.693\left(\frac{t}{A\varepsilon^{p}\exp\left(\frac{Q}{RT}\right)}\right)^{n}\right], \quad (1)$$

where t is the annealing time, and $X(t)$ is defined as the ratio of the recrystallized grain area to the total grain area. Here, A is a material constant, ε is the equivalent plastic strain, p is the strain sensitivity exponent, Q is the activation energy

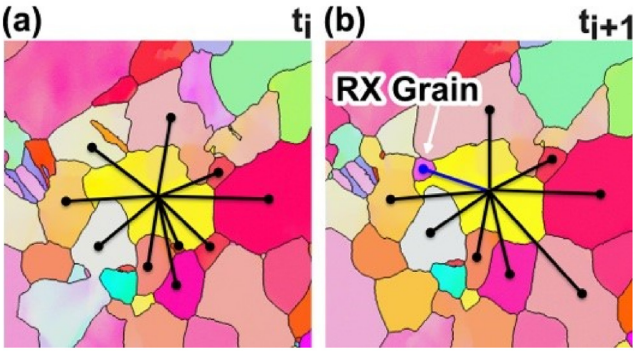


Fig. 7. Identification of recrystallized grains using a graph–based approach: (a) grain orientation map at annealing step $t = t_i$, highlighting a representative grain and its neighboring grains; (b) grain orientation map at the subsequent annealing step $t = t_{i+1}$, exhibiting the same grain and its updated neighborhood. The newly recrystallized grain is indicated by a white arrow.

for static recrystallization, R is the universal gas constant, and T is the absolute temperature [43]. The Avrami exponent, n reflects the rate and nature of the nucleation and growth of recrystallization during annealing [49]. The JMAK fit to the experimental data, given by Eq. (1), is shown as a solid blue line in Fig. 10. The fit was obtained using the parameters $n = 0.8$, $p = 1$, $A = 1.425 \times 10^{-4}$ s, $Q = 100.5$ kJ mol^{-1}, and $\varepsilon = 0.05$, evaluated at $T = 573.15$ K (300 °C), with $R = 8.314$ J mol^{-1}K^{-1}. This parameter set does not represent a unique solution; however, it is provided as a visual guide to exhibit the overall trend. The red-filled circles represent the recrystallized fraction, determined using a graph–based approach for identifying recrystallized grains. The recrystallized fraction is defined as the ratio of recrystallized grain area to total grain area.

As shown in Fig. 10, recrystallization initially follows the JMAK fit up to approximately 20% recrystallization. Beyond this point, the nucleation rate decreases, and the process transitions toward a saturation regime, leading to a deviation from the JMAK model. The initial rapid recrystallization is attributed to the high stored energy introduced by plastic deformation during plane strain compression. The saturation regime is characterized by slower recrystallization kinetics, which can be attributed to the progressive reduction in stored energy associated with the depletion of twinned structures and general overall recovery. In addition, solute drag reduces grain boundary mobility, further retarding the recrystallization in Mg–Zn–Ca alloy, as reported by Zeng et al. [17] for cold-rolled Mg–Zn–Ca alloys and described by Montiel et al. [48] for hot-compressed ZX30. To confirm the saturation regime, the *in situ* sample was subjected to an additional 4 h of annealing at 300 °C. No further increase in the recrystallized fraction was observed, which remained at approximately 28%.

4.2. Preferential recrystallization at grain boundaries

To determine whether recrystallization occurred preferentially at grain boundaries, triple or quadruple junctions, the number of grains neighboring each newly recrystallized grain was quantified at each time step. The newly recrystallized grains that were not in contact with twin boundaries at each annealing step are cumulatively shown in Fig. 11(a). The number of the neighboring grains is represented by five distinct colors. Based on the cumulative distribution of newly recrystallized grains over the entire annealing process, 36% of the recrystallized grains have three neighboring grains, followed by 28% with two neighbors, 22% with four neighbors, and 10% with five neighbors. The cumulative number of newly recrystallized grains is also shown in the column chart in Fig. 11(b). Although this statistic suggests that recrystallized grains are most frequently associated with triple junctions, it does not necessarily indicate that nucleation occurs precisely at these locations. This analysis reflects not only nucleation events but also post-nucleation grain growth and resulting interactions between neighboring grains. Within these limitations, triple-junctions were determined to be the most frequently observed topology.

4.3. Preferential recrystallization near twins

A twinning analysis was performed using the MTEX toolbox in MATLAB. The analysis reveals that the dominant twin mode is $\{10\bar{1}2\}\langle 10\bar{1}1\rangle$ tensile twinning, which is characterized by a 86° lattice rotation about the $\langle 11\bar{2}0\rangle$ axis. The neighboring grains of a highly twinned grain were examined in detail, as illustrated in Fig. 6(a–e). The parent grain, E, is progressively consumed by the surrounding grains as annealing proceeds. As shown from Fig. 6(a) to Fig. 6(e), the grain progressively dissociates from the twin planes, and the former twin boundaries evolve into new grain boundaries of the remaining grain. The grain is no longer traceable by the end of the process as shown in Fig. 6(e), as the twinned structure is depleted and the remaining grain interior is progressively consumed.

An orientation map corresponding to the annealing step at $t = 9.2$ min, with the twin boundaries highlighted in white, is shown in Fig. 12(a) as an illustrative example. The boundaries of newly recrystallized grains at this stage are outlined in thick black lines. As illustrated in Fig. 12(a), three recrystallized grains nucleate and evolve along grain boundaries, while three additional recrystallized grains are observed adjacent to a twin boundary.

To investigate whether or not twin boundaries act as preferential nucleation sites for recrystallization, two metrics are used in Fig. 12(b): (i) the ratio of the number of newly recrystallized grains touching a twin boundary to the total number of recrystallized grains, and (ii) the fraction of twin boundary length relative to the total grain boundary length. The former indicates how many recrystallized grains formed near a twin boundary, and the latter indicates the prevalence of twin boundaries in the microstructure. The results show that approximately 70% of the early recrystallized grains nucleated adjacent to the twin boundaries. At this same time step ($t = 1$ min), only 40% of the available grain boundaries are classified as twin boundaries. Together, these observations suggest that recrystallization preferentially occurs

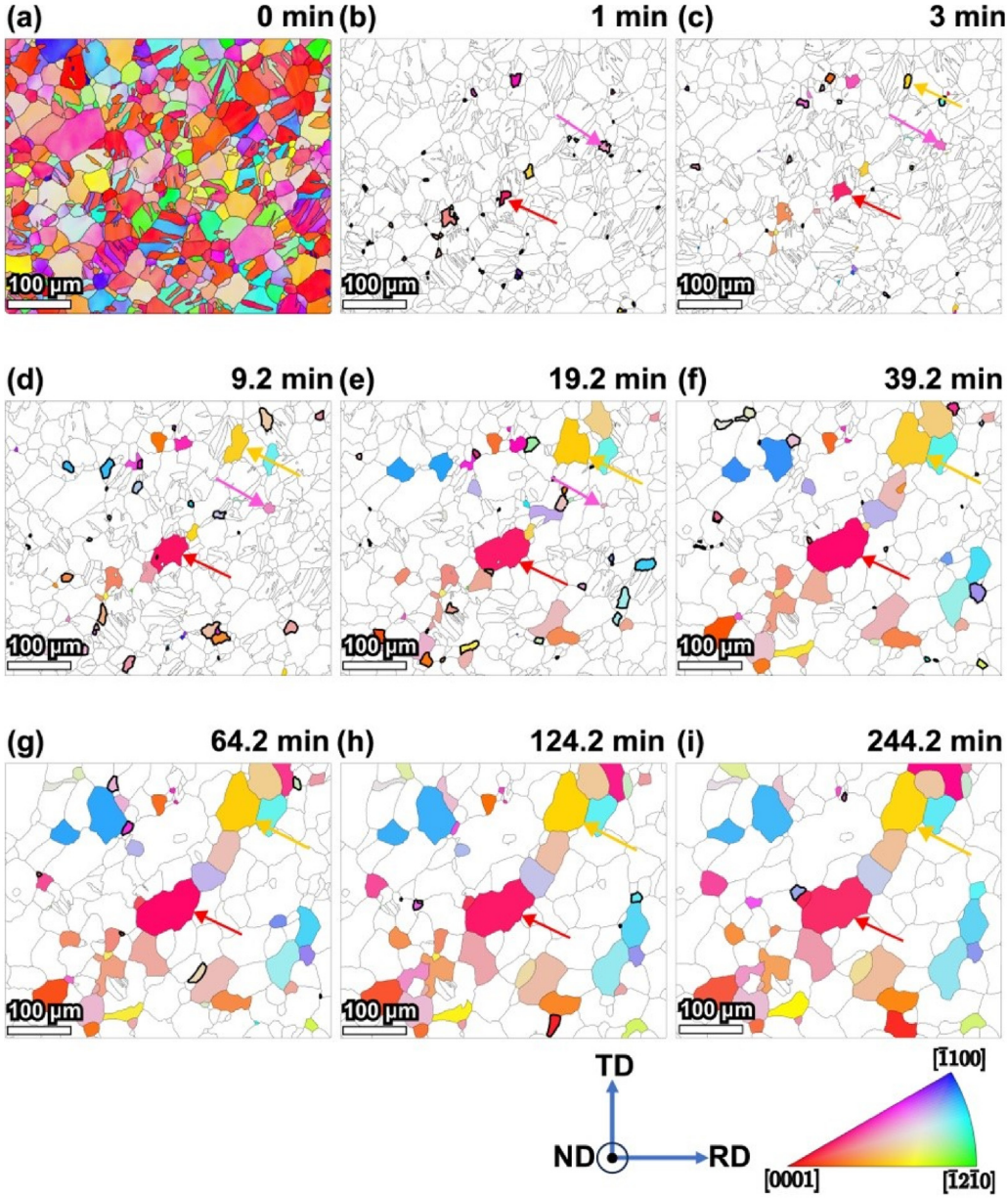


Fig. 8. EBSD IPF–Z maps showing recrystallized grain evolution. Grains are colored according to crystallographic orientation with respect to the normal direction (ND), as indicated by the IPF color key. Newly recrystallized grains at each annealing step are highlighted by their grain boundaries. The corresponding annealing steps are: (a) $t = 0$ min (unheated); (b) $t = 1$ min; (c) $t = 3$ min; (d) $t = 9.2$ min; (e) $t = 19.2$ min; (f) $t = 39.2$ min; (g) $t = 64.2$ min; (h) $t = 124.2$ min; (i) $t = 244.2$ min.

at twin boundaries versus grain boundaries. However, after the third annealing stage ($t = 9.2$ min), only approximately 40% of the newly recrystallized grains remained in contact with twin boundaries, indicating a progressive reduction in the influence of twin boundaries as recrystallization and grain growth proceeded. During annealing, both metrics decreased as the twin boundaries were consumed. However, the percentage of new recrystallized grains on twin boundaries is consistently higher than the percentage, or availability, of twin boundaries versus grain boundaries.

4.4. Grain orientation spread (GOS)

Grain Orientation Spread (GOS) is a measure that quantifies the orientation variation within a grain. After determining the mean orientation of a grain, the misorientation of each pixel within that grain relative to this mean orientation is calculated. These misorientation values are then averaged by normalizing their sum with respect to the total number of pixels in the grain, yielding a single representative GOS value assigned to that grain.

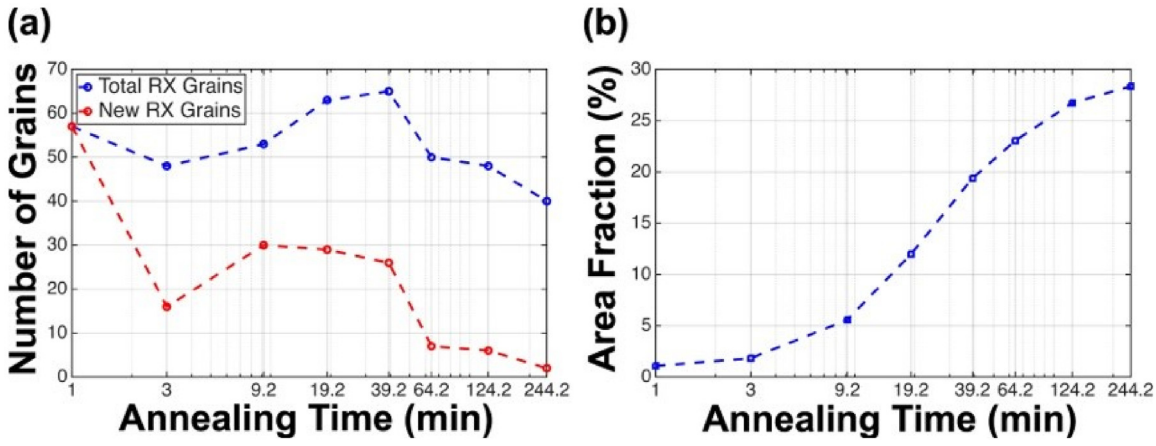


Fig. 9. Number and area fraction of recrystallized grains at each annealing step: (a) comparison of the total number of recrystallized grains and the number of newly nucleated recrystallized grains; (b) the area fractions (%) of total recrystallized grains.

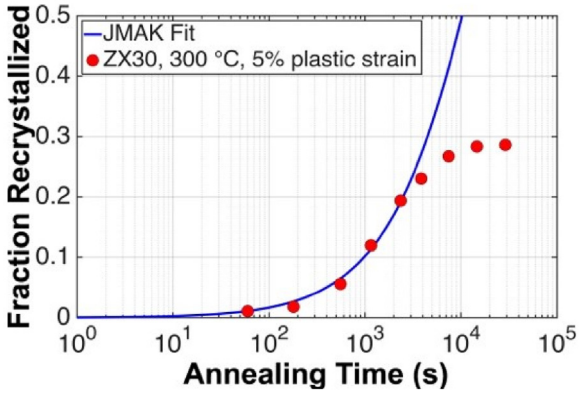


Fig. 10. Recrystallization kinetics during annealing of the Mg–Zn–Ca alloy at 300 °C. Recrystallized fraction as a function of annealing time, with time plotted on a logarithmic scale, determined from graph–based analysis.

GOS has been extensively used as a criterion to determine the number and area fraction of recrystallized grains from EBSD. This criterion typically assumes that grains with a GOS value $<1°$ are recrystallized grains. To test this criterion, GOS maps were obtained corresponding to each annealing step employing the MTEX toolbox in MATLAB as illustrated in Fig. 13(a–i). The measured GOS values are divided into four intervals as shown in the legend: light blue (0°–1°), green (1°–2°), yellow (2°–5°), and orange (5°–10°) orientation spread. On the same maps, the boundaries of the recrystallized grains that we identified using the graph–based approach are outlined in red. This visualization shows that the GOS values of the recrystallized grains are mostly $<1°$, but it also reveals that the GOS values of many non-recrystallized grains are also $<1°$.

To quantitatively analyze this, Table 1 was constructed to report the number percentages of (i) recrystallized grains with GOS $\leq$ 1°, (ii) recrystallized grains with GOS $>1°$, (iii) non-recrystallized grains with GOS $\leq$ 1°, and (iv) non-recrystallized grains with GOS $>1°$. The results indicate that, as annealing progresses and recrystallization begins to slow

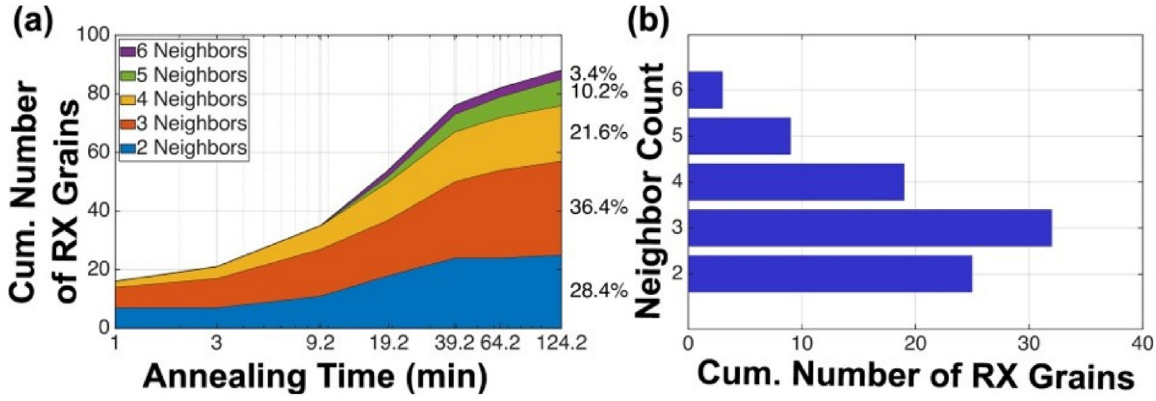


Fig. 11. Evolution of the neighborhood topology of recrystallized grains which are not touching twin boundaries: (a) Stacked area chart showing the cumulative number of recrystallized grains as a function of annealing time. The contributions from recrystallized grains with different numbers of neighboring grains (2, 3, 4, 5, and 6 neighbors) are shown. The observed neighborhood configurations may reflect both the initial nucleation sites and subsequent grain growth interactions during recrystallization; (b) Column chart showing the cumulative number of recrystallized grains classified by their number of neighboring grains (2–6).

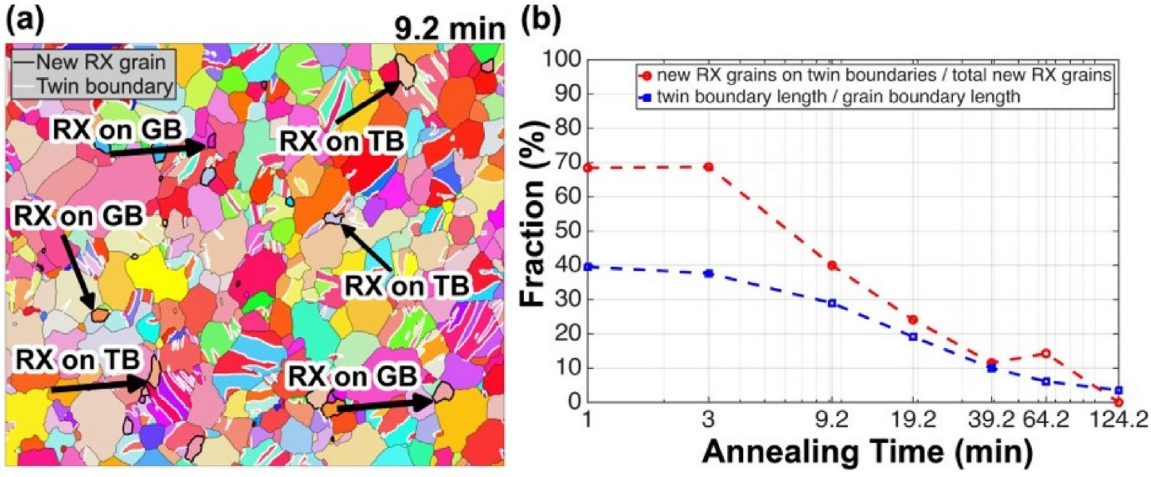


Fig. 12. Recrystallized grains associated with twin boundaries and grain boundary during annealing: (a) outlined recrystallized grains (RX) at the annealing step $t = 9.2$ min. Selected recrystallized grains touching twin boundaries (TB) and grain boundaries (GB), indicated by black arrows. Twin boundaries are highlighted in white. (b) Quantitative metrics used to assess twin boundaries as preferred nucleation sites for recrystallized grains. The annealing time is plotted on a logarithmic scale.

Table 1
Number percentage distribution of recrystallized and non-recrystallized grains with GOS values below and above the 1° threshold at different annealing times.

Process step	Recrystallized grains (%)		Non-recrystallized grains (%)	
	GOS $\leq$ 1°	GOS $>$ 1°	GOS $\leq$ 1°	GOS $>$ 1°
t = 1 min	82.5	17.5	45.3	54.7
t = 3 min	81.2	18.8	46.2	53.8
t = 9.2 min	81.1	18.9	51.1	48.9
t = 19.2 min	85.7	14.3	56.0	44.0
t = 39.2 min	96.9	3.1	61.3	38.7
t = 64.2 min	98.0	2.0	69.4	30.6
t = 124.2 min	95.8	4.2	77.8	22.2
t = 244.2 min	95.0	5.0	85.9	14.1

down ($t = 64.2$ min), approximately 98% of recrystallized grains exhibit GOS $\leq$ 1°. However, nearly 70% of non-recrystallized grains also fall within GOS $\leq$ 1°, suggesting that low GOS alone is not sufficient to uniquely distinguish fully recrystallized regions, at least for the conditions investigated here. The occurrence of low GOS values in non-recrystallized grains is attributed to recovery processes, particularly at later stages of annealing, where intragranular misorientation is substantially reduced even within non-recrystallized grains. In addition, high GOS is associated with high deformation. Since the amount of strain was only 5%, some grains may have been only lightly distorted, resulting in low GOS values and a low driving force for recrystallization.

The evolution of the area fraction of grains with GOS $\leq$ 1° and GOS $\leq$ 2° was examined throughout the annealing process as shown in Fig. 14. The area fraction of the grains with GOS $\leq$ 1° increases progressively with annealing time, reaching 90% by the end of the annealing process. Furthermore, all grains examined in the field of view exhibit GOS values of $\leq$ 2° at the final annealing stage. As also shown in Fig. 14, the area fraction of recrystallized grains remains substantially lower than the area fraction of grains with GOS $\leq$ 1° throughout the annealing process.

The analysis reveals that, although GOS has been widely employed as a scalar criterion for identifying recrystallized grains, the assumption of a fixed threshold (commonly GOS $\leq$ 1°) is not sufficiently robust for reliable classification, at least under the low strain and high temperature conditions investigated here. However, the area fraction of grains with GOS $\leq$ 1° may still serve as a useful indicator of the grain growth of lightly deformed grains. It should be noted that this metric captures the effects of recovery, recrystallization, and the grain growth of lightly deformed grains, rather than solely recrystallization.

4.5. Kernel average misorientation (KAM)

Kernel Average Misorientation (KAM) is defined as the average misorientation between a given pixel and its neighboring pixels. It serves as a measure of local lattice curvature and is widely used as an indicator of defect density, particularly geometrically necessary dislocations (GNDs).

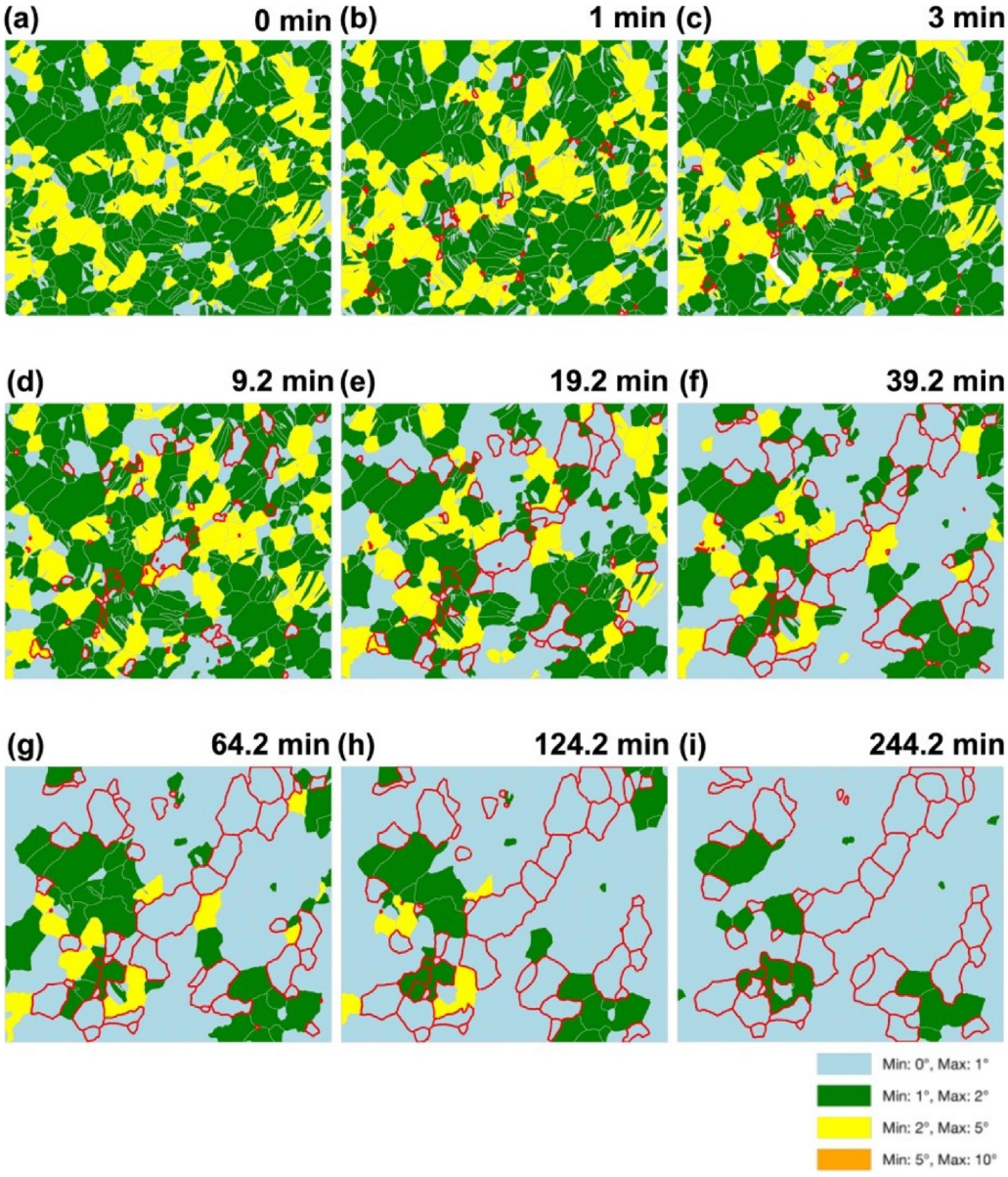


Fig. 13. Grain orientation spread (GOS) maps corresponding to successive annealing steps, with the grain boundaries of recrystallized grains highlighted. The corresponding annealing times are: (a) $t = 0$ min (unheated); (b) $t = 1$ min; (c) $t = 3$ min; (d) $t = 9.2$ min; (e) $t = 19.2$ min; (f) $t = 39.2$ min; (g) $t = 64.2$ min; (h) $t = 124.2$ min; (i) $t = 244.2$ min.

KAM maps are presented in Fig. 15(a–i) employing the MTEX toolbox in MATLAB. The recrystallized grains, as determined via graph-based approach, are outlined in red. Regions shown in yellow/green correspond to high KAM values, indicating elevated lattice distortion and high stored energy, whereas deep blue regions, with KAM values approaching 0°, exhibit minimal lattice distortion and represent highly recovered or lightly deformed grains. At the initial annealing stages as shown in Fig. 15(b–c), a heterogeneous strain field is observed, predominantly concentrated near twin boundaries, as reflected by the high average KAM values. Between 9.2 min and 19.2 min, as shown in Fig. 15(d–e), discrete deep blue regions (KAM = 0°) progressively expand over time. Concurrently, grain boundaries move to consume the surrounding deformed grains. From 64.2 min to 244.2 min, as shown in Fig. 15(g–i), the field of view becomes predominantly deep blue. At this stage, the driving force arising from strain energy and grain boundary energy is largely exhausted. The recrystallized grains, highlighted by red boundaries, no longer exhibit significant growth.

This analysis reveals that KAM does not provide a definitive scalar threshold for the identification and quantification of recrystallized grains. Although deep blue regions (KAM = 0°) are typically associated with strain-free recrystallized grains, strain-free grains that were not identified as recrystallized were also observed during the intermediate annealing stages, as indicated by the arrows in Fig. 15(d–h).

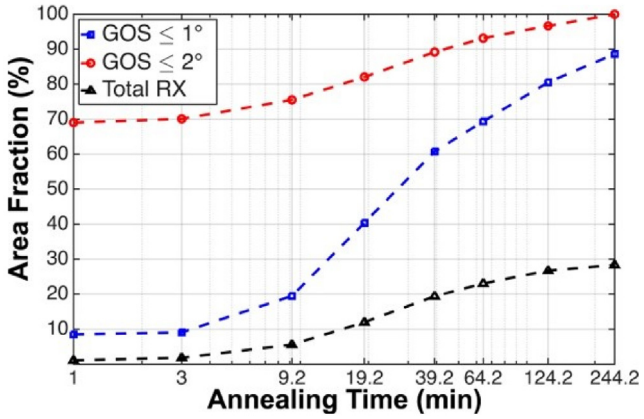


Fig. 14. Area fractions of grains with GOS ≤ 1°, GOS ≤ 2°, and total recrystallized grains as a function of annealing time.

4.6. Texture analysis

Texture analysis was performed to quantify the basal intensity (i.e., how strong the basal texture is) throughout the annealing process, as shown in Fig. 16(a–i). The basal intensity decreases with the annealing time, reaching a minimum at $t = 19.2$ min, as illustrated in Fig. 16(e). This reduction indicates the weakening of the basal texture, which is favorable for improving the formability of the Mg–Zn–Ca alloy. However, the basal intensity begins to increase again after $t = 19.2$ min and reaches a maximum value at the end of the process, as shown in Fig. 16(i). Nevertheless, it is not clear whether this texture evolution is representative, as the texture analysis becomes less statistically significant due to the decreasing number of grains as annealing progresses. Statistically meaningful texture characterization typically requires at least 500 grains; however, this criterion could not be met in the present analysis. After the fourth annealing step, fewer than 300 grains remained within the field of view, and by the end of recrystallization, only approximately 150 grains were present. Consequently, the pole figures became increasingly dominated by a small number of large grains. These grains happen to possess basal orientations; consequently, as annealing and grain growth proceed, the texture appears to become more basal in nature.

To further analyze the unexpected increase in the basal intensity, inverse pole figures in which individual grains are indicated are shown in Fig. 17(a–i). Each bubble represents an individual grain, and the bubble size is proportional to

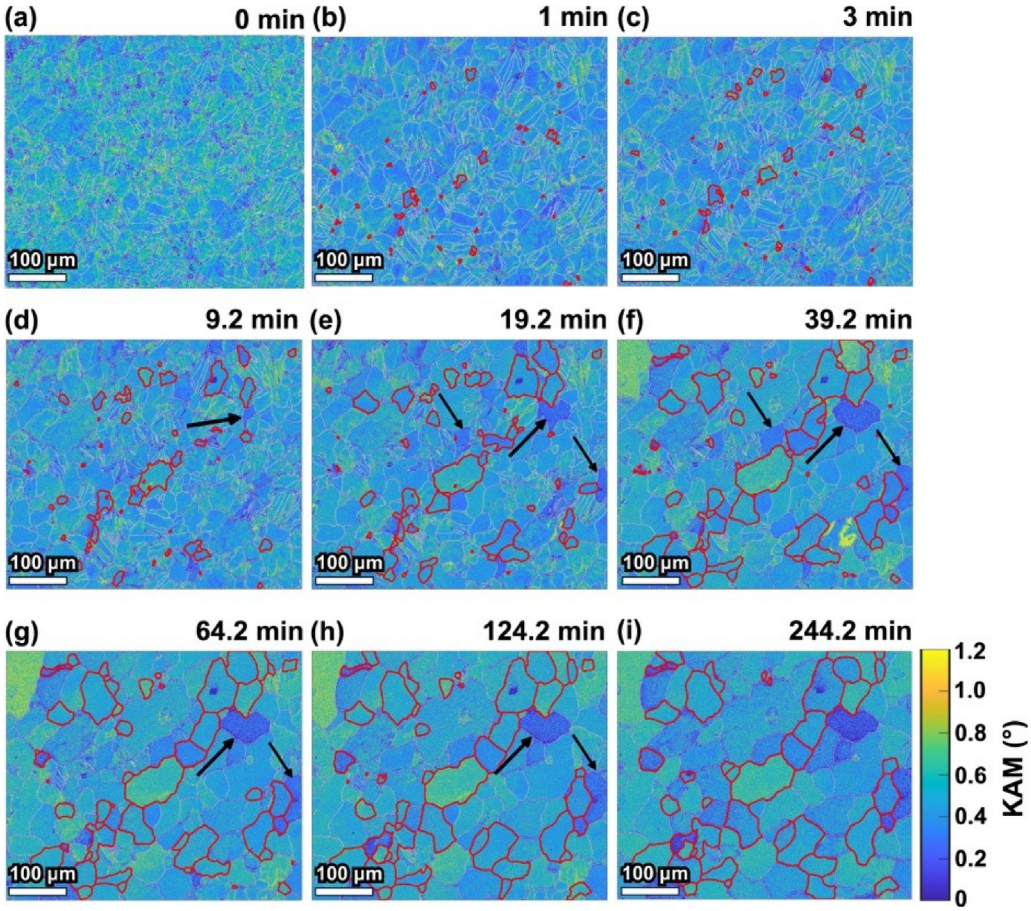


Fig. 15. Kernel average misorientation (KAM) maps corresponding to successive annealing steps, with the grain boundaries of recrystallized grains highlighted. The corresponding annealing times are: (a) $t = 0$ min (unheated); (b) $t = 1$ min; (c) $t = 3$ min; (d) $t = 9.2$ min; (e) $t = 19.2$ min; (f) $t = 39.2$ min; (g) $t = 64.2$ min; (h) $t = 124.2$ min; (i) $t = 244.2$ min.

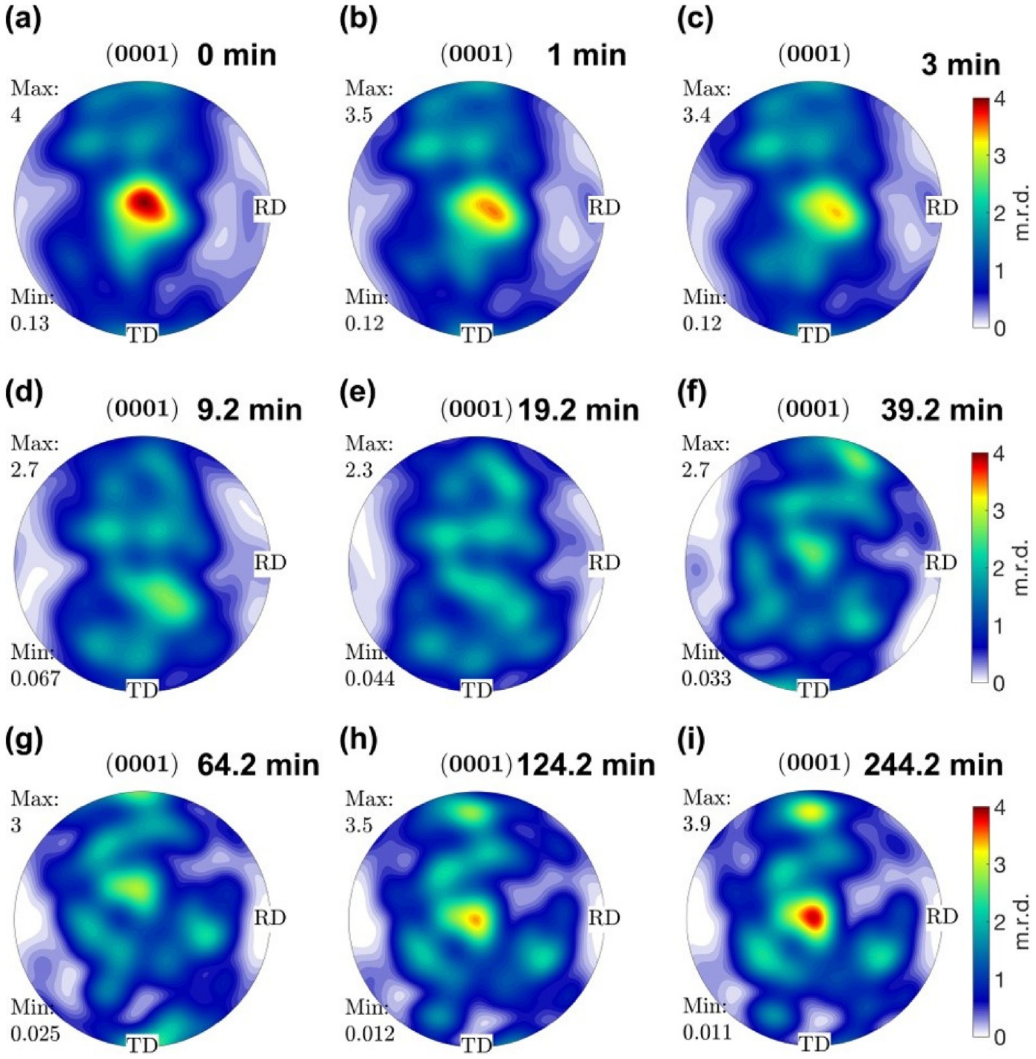


Fig. 16. Basal pole figures corresponding to successive annealing steps. The corresponding annealing times are: (a) $t = 0$ min (unheated); (b) $t = 1$ min; (c) $t = 3$ min; (d) $t = 9.2$ min; (e) $t = 19.2$ min; (f) $t = 39.2$ min; (g) $t = 64.2$ min; (h) $t = 124.2$ min; (i) $t = 244.2$ min.

the grain area. Red denotes orientations aligned close to the basal pole, whereas green and blue correspond to orientations near the prismatic poles. At the initial stage, as shown in Fig. 17(a), the red circles are densely concentrated around the basal pole [0001], and a fine-grained microstructure is evident in Fig. 17(a–d). From Fig. 17(b) through Fig. 17(i), the total grain count decreases drastically as the smaller grains are progressively consumed by the moving grain boundaries. Concurrently, the average size of the surviving circles (grains) increases significantly. As illustrated in Fig. 17(i), the microstructure becomes dominated by a small number of large grains.

This analysis indicates that the development and growth of off-basal orientations contribute to texture weakening (or randomization), a critical phenomenon for enhancing the formability and ductility of Mg alloys during static recrystallization. The late strengthening of the basal texture as shown in Fig. 16 comes from these few but relatively large basal grains and the small population size (i.e., small for an accurate texture analysis) that occurs in the later part of the annealing process.

To investigate the weakening of the basal texture, the total number of grains and the number of recrystallized grains are plotted as a function of the angle between the basal c-axis ([0001] direction) and the ND, as shown in Fig. 18(a–b). As illustrated in Fig. 18(a), the alloy system exhibits a bimodal texture from $t = 0$ min to $t = 9.2$ min, with grains concentrated around a peak at approximately 25°−30° from the ND, and a second broader peak in the range of 65°−90°. As annealing progresses, the total number of grains progressively decreases, indicating ongoing grain growth in which larger grains consume smaller ones to reduce the overall grain boundary energy of the system. With increasing annealing time, particularly for $t > 39.2$ min, the bimodal distribution becomes less pronounced. By $t = 244.2$ min, the grain orientation distribution approaches a nearly uniform state, suggesting that continued grain growth leads to texture randomization.

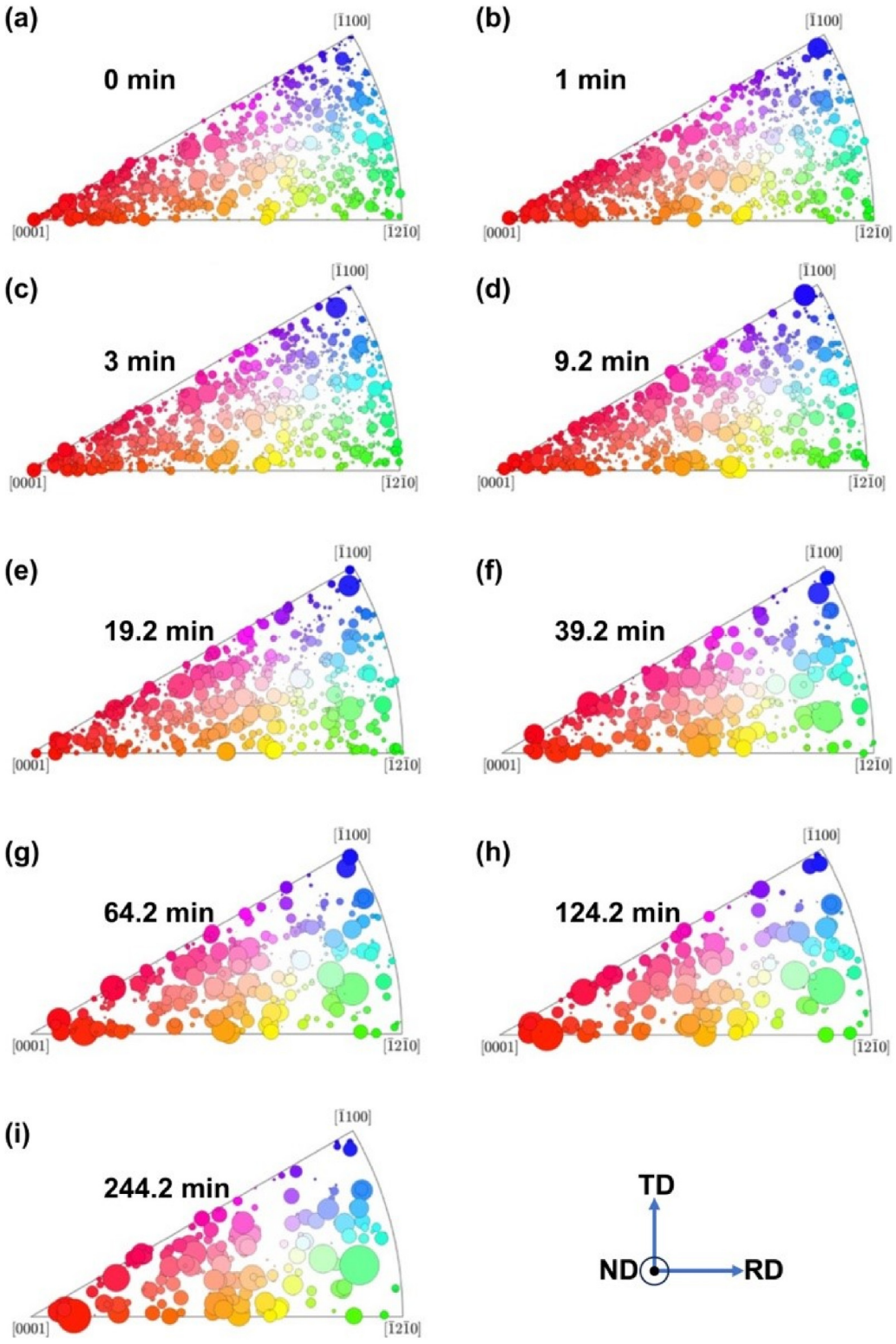


Fig. 17. Individual grains are indicated as bubbles within the inverse pole figure (IPF) for successive annealing steps. The corresponding annealing times are: (a) $t = 0$ min (unheated); (b) $t = 1$ min; (c) $t = 3$ min; (d) $t = 9.2$ min; (e) $t = 19.2$ min; (f) $t = 39.2$ min; (g) $t = 64.2$ min; (h) $t = 124.2$ min; (i) $t = 244.2$ min.

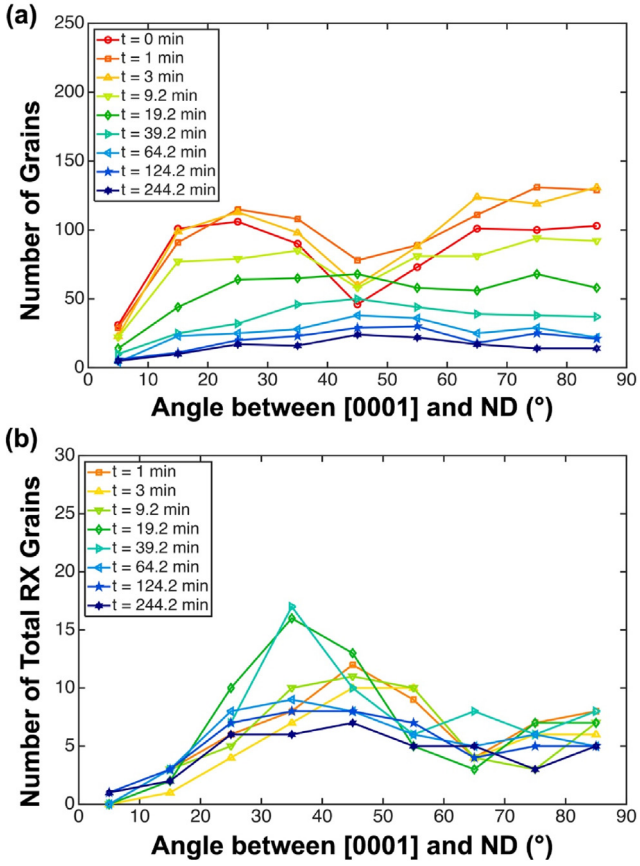


Fig. 18. Evolution of the angle between the c-axis and the normal direction (ND) during the annealing process: (a) distribution for all grains at each annealing step, (b) distribution for recrystallized (RX) grains at each annealing step.

Fig. 18(b) shows that, in contrast to the total grain number, the recrystallized (RX) grains exhibit a distinct single-peak preferred orientation. This peak consistently forms within an angular range of 35°−55° from the ND for the first three annealing steps. This behavior indicates that the nucleation of strain-free recrystallized grains is strongly favored within this specific crystallographic orientation window. This finding is significant because it indicates that the desired texture weakening indeed comes from the contribution of the recrystallized grains. Furthermore, this observation is only possible using *in situ* EBSD where the true recrystallized grains can be identified by way of grain tracking.

The number of RX grains within the 35°−45° peak increases with annealing time, reaching a maximum at $t = 39.2$ min. Beyond 39.2 min, the total number of RX grains begins to decrease, while the peak simultaneously becomes broader, indicating a progressive spread in the orientation distribution of recrystallized grains. These findings are consistent with the results reported by Roumina et al. [20] for ZX30 subjected to 20% deformation and annealing at 230 °C. In that study, recrystallized grains were observed to nucleate over a broader preferred orientation range (30°−60°), accompanied by faster recrystallization kinetics and a higher number of recrystallized grains.

5. Conclusion

The static recrystallization behavior of the Mg–Zn–Ca (ZX30) alloy, deformed to 5% strain at 200 °C, was systematically investigated in this study by employing *in situ* EBSD characterization during successive annealing increments at 300 °C. The recrystallized grains were identified, tracked, and quantitatively analyzed using a graph-based approach. The findings of this study are summarized as follows:

1. The number of grains was reduced to nearly one-third of the initial count over 244 min of annealing. The average grain diameter doubled by the end of the overall annealing process. The initial twin structures were nearly depleted at the final stage.
2. Throughout the annealing process, the number of newly nucleated recrystallized grains decreases at each step. After 20 min of annealing, the number of recrystallized grains decreases to nearly 100. At the end of the process, the cumulative recrystallized grain area accounted for only 28% of the total grain area.
3. The results revealed a prevalence for recrystallization adjacent to twin boundaries with ∼70% of early recrystallized grains appearing on twin boundaries, despite twin boundary length accounting for only ∼40% of the total grain boundary length. However, as the annealing progressed and the twin structures were gradually depleted, this fraction in turn decreased.
4. The recrystallized grains that were not in contact with twin boundaries were also quantitatively analyzed. The results indicate that recrystallization occurs at different grain boundary configurations with varying frequencies. Among these, triple junctions represented the most common configuration, accounting for approximately 36% of the recrystallized grains not adjacent to twin boundaries. The predominance of triple junctions should not be interpreted solely as evidence of preferential nucleation at triple junctions, but also as a consequence of subsequent grain growth and grain boundary interactions.
5. The analysis demonstrates that Grain Orientation Spread (GOS) $\leq 1°$, although conventionally used as a metric for identifying recrystallized grains, does not provide a uniquely reliable threshold for recrystallized grain classification for the low strain condition investigated here. While GOS is not sufficiently discriminative for precise phase identification on a grain-by-grain basis, it remains a useful macroscopic indicator for tracking the reduction of stored energy due to the combined effects of recrystallization and recovery.
6. The analysis revealed that while KAM effectively captures the evolution of local lattice distortion and dislocation activity during annealing, it does not provide a unique or physically robust indicator of recrystallized grains.

The grain orientation distributions indicate that most recrystallized grains develop broadly distributed, nearly random orientations during static recrystallization. While the pole fig-

ures show a partial increase in basal texture intensity at later stages of annealing, this behavior is mainly caused by the growth of a limited number of large basal-oriented grains. Thus, the increase in pole figure intensity does not reflect a uniform strengthening of basal texture among the recrystallized grains. Instead, recrystallization produces a broad range of grain orientations, with the measured texture response being strongly influenced by the size and growth behavior of a small subset of grains. This distinction is only accessible through in situ EBSD, where individual recrystallized grains can be identified and tracked throughout annealing.

Declaration of competing interest

The authors declare that they have no known competing financial interests or personal relationships that could have appeared to influence the work reported in this paper.

CRediT authorship contribution statement

Abdulhamit Sarac: Writing – review & editing, Writing – original draft, Software, Methodology, Investigation, Data curation, Conceptualization. **Tracy Berman:** Writing – review & editing, Methodology, Investigation, Data curation, Conceptualization. **Varun S. Venkatesh:** Writing – review & editing, Software, Methodology, Investigation. **Ashwin J. Shahani:** Writing – review & editing, Software, Methodology. **John Allison:** Writing – review & editing, Methodology, Funding acquisition, Conceptualization. **Ashley Bucsek:** Writing – review & editing, Methodology, Funding acquisition, Conceptualization.

Acknowledgments

AS, TB, JA, and AB were supported by the U.S. Department of Energy Office of Basic Energy Sciences, Division of Materials Science and Engineering, under Award DE-SC0008637 as part of the Center for Predictive Integrated Structural Materials Science (PRISMS). VSV and AJS acknowledge support from the Army Research Office, United States, under Grant No. W911NF-22-2-0057.

References

[1] J. Bohlen, M.R. Nürnberg, J.W. Senn, D. Letzig, S.R. Agnew, Acta Mater. 55 (2007) 2101–2112, doi:10.1016/j.actamat.2006.11.013.
[2] L.W. Mackenzie, M.O. Pekguleryuz, Scr Mater. 59 (2008) 665–668, doi:10.1016/j.scriptamat.2008.05.021.
[3] K. Hantzsche, J. Bohlen, J. Wendt, K.U. Kainer, S.B. Yi, D. Letzig, Scr Mater. 63 (2010) 725–730, doi:10.1016/j.scriptamat.2009.12.033.
[4] I. Basu, T. Al-Samman, G. Gottstein, Mater. Sci. Eng.: A 579 (2013) 50–56, doi:10.1016/j.msea.2013.04.076.
[5] I. Basu, T. Al-Samman, Acta Mater. 67 (2014) 116–133, doi:10.1016/j.actamat.2013.12.015.
[6] M. Sanjari, A. Farzadfar, A.S. Kabir, H. Utsunomiya, I.H. Jung, R. Petrov, L. Kestens, S. Yue, J. Mater. Sci. 49 (2014) 1408–1425, doi:10.1007/s10853-013-7826-3.
[7] H. Ding, X. Shi, Y. Wang, G. Cheng, S. Kamado, Mater. Sci. Eng.: A 645 (2015) 196–204, doi:10.1016/j.msea.2015.08.025.
[8] L.Y. Zhao, H. Yan, R.S. Chen, E.H. Han, Scr Mater. 188 (2020) 200–205, doi:10.1016/j.scriptamat.2020.07.037.
[9] L.Y. Zhao, H. Yan, R.S. Chen, E.H. Han, J. Magnes. Alloys 9 (2021) 818–828, doi:10.1016/j.jma.2020.02.026.
[10] H. Liu, S. Zhu, T.B. Abbott, Z. Zhen, J.F. Nie, JOM 74 (2022) 2592–2608, doi:10.1007/s11837-022-05321-0.
[11] F. Mouhib, B. Gao, T. Al-Samman, J. Mater. Sci. 59 (2024) 1044–1055, doi:10.1007/s10853-023-09243-3.
[12] N. Stanford, M. Barnett, Scr Mater. 58 (2008) 179–182, doi:10.1016/j.scriptamat.2007.09.054.
[13] J.P. Hadorn, K. Hantzsche, S. Yi, J. Bohlen, D. Letzig, J.A. Wollmershauser, S.R. Agnew, Metall. Mater. Trans. A: Phys. Metall. Mater. Sci. 43 (2012) 1347–1362, doi:10.1007/s11661-011-0923-5.
[14] F. Mouhib, R. Pei, B. Erol, F. Sheng, S. Korte-Kerzel, T. Al-Samman, Mater. Sci. Eng.: A 847 (2022) 143348, doi:10.1016/j.msea.2022.143348.
[15] A.G. Beer, M.R. Barnett, Metall. Mater. Trans. A: Phys. Metall. Mater. Sci. 38 (2007) 1856–1867, doi:10.1007/s11661-007-9207-5.
[16] D.W. Kim, B.C. Suh, M.S. Shim, J.H. Bae, D.H. Kim, N.J. Kim, Metall. Mater. Trans. A: Phys. Metall. Mater. Sci. 44 (2013) 2950–2961, doi:10.1007/s11661-013-1674-2.
[17] Z.R. Zeng, Y.M. Zhu, S.W. Xu, M.Z. Bian, C.H. Davies, N. Birbilis, J.F. Nie, Acta Mater. 105 (2016) 479–494, doi:10.1016/j.actamat.2015.12.045.
[18] J. Luo, H. Yan, N. Zheng, R.S. Chen, Acta Metall. Sin. (Engl. Lett.) 29 (2016) 205–216, doi:10.1007/s40195-016-0378-1.
[19] T.D. Berman, J.E. Allison, JOM 73 (2021) 1450–1459, doi:10.1007/s11837-021-04630-0.
[20] R. Roumina, S. Lee, T.D. Berman, K.S. Shanks, J.E. Allison, A. Bucsek, Acta Mater. 234 (2022) 118039, doi:10.1016/j.actamat.2022.118039.
[21] X. Wang, D. Guan, J. Magnes. Alloys 10 (2022) 1235–1241, doi:10.1016/j.jma.2021.08.026.
[22] T.D. Berman, J.E. Allison, in: Minerals, Metals and Materials Series, Springer Science and Business Media Deutschland GmbH, 2023, pp. 19–21, doi:10.1007/978-3-031-22645-8_5.
[23] R. Gomez, A. Leonard, Microsc. Microanal. 30 (Suppl 1) (2024) 648, doi:10.1093/mam/ozae044.306.
[24] R. Roumina, S. Lee, T.D. Berman, K.S. Shanks, J.E. Allison, A. Bucsek, Metall. Mater. Trans. A: Phys. Metall. Mater. Sci. 56 (2025) 3788–3801, doi:10.1007/s11661-025-07884-4.
[25] J. Bohlen, J. Wendt, M. Nienaber, K.U. Kainer, L. Stutz, D. Letzig, Mater. Charact. 101 (2015) 144–152, doi:10.1016/j.matchar.2015.02.002.
[26] T. Al-Samman, K.D. Molodov, D.A. Molodov, G. Gottstein, S. Suwas, Acta Mater. 60 (2012) 537–545, doi:10.1016/j.actamat.2011.10.013.
[27] D. Guan, W.M. Rainforth, J. Gao, L. Ma, B. Wynne, Acta Mater. 145 (2018) 399–412, doi:10.1016/j.actamat.2017.12.019.
[28] I. Basu, T. Al-Samman, Acta Mater. 96 (2015) 111–132, doi:10.1016/j.actamat.2015.05.044.
[29] J. Shi, K. Cui, B. Wang, L. Deng, C. Wang, Z. Xu, Q. Li, Mater. Charact. 129 (2017) 104–113, doi:10.1016/j.matchar.2017.04.029.
[30] X. Ye, Z. Suo, Z. Heng, B. Chen, Q. Wei, J. Umeda, K. Kondoh, J. Shen, J. Magnes. Alloys 12 (2024) 1419–1430, doi:10.1016/j.jma.2023.01.021.
[31] B. Zhang, Y. Wang, L. Geng, C. Lu, Mater. Sci. Eng.: A 539 (2012) 56–60, doi:10.1016/j.msea.2012.01.030.
[32] J. Zhang, Y. Dou, G. Liu, Z. Guo, Comput. Mater. Sci. 79 (2013) 564–569, doi:10.1016/j.commatsci.2013.07.012.
[33] H. Wang, D. Zhang, C. Qiu, D. Chen, Trans. Nonferrous Met. Soc. China (Engl. Ed.) 35 (2025) 1456–1470, doi:10.1016/S1003-6326(24)66760-9.
[34] R.A. Gomez, D.P. Veghte, D.J. Rowenhorst, B.W. Williams, A.D. Murphy-Leonard, J. Magnes. Alloys 15 (2026) 101945, doi:10.1016/j.jma.2025.10.026.
[35] F.J. Humphreys, M. Ferry, Mater. Sci. Forum 217-222 (1996) 529–534, doi:10.4028/www.scientific.net/msf.217-222.529.
[36] P.J. Hurley, F.J. Humphreys, J. Microsc. 213 (2004) 225–234, doi:10.1111/j.0022-2720.2004.01300.x.

[37] Y. Huang, F.J. Humphreys, Mater. Chem. Phys. 132 (2012) 166–174, doi:10.1016/j.matchemphys.2011.11.018.
[38] A. Chakkedath, D.H. Escobar, J. Bohlen, S. Yi, D. Letzig, C. Boehlert, in: A. Singh, K. Solanki, M.V. Manuel, N.R. Neelameggham (Eds.), TMS 2016 Supplemental Proceedings, John Wiley & Sons, 2016, pp. 237–238.
[39] D. Guan, W.M. Rainforth, J. Gao, J. Sharp, B. Wynne, L. Ma, Acta Mater. 135 (2017) 14–24, doi:10.1016/j.actamat.2017.06.015.
[40] M.G. Jiang, C. Xu, H. Yan, T. Nakata, Z.W. Chen, C.S. Lao, R.S. Chen, S. Kamado, E.H. Han, J. Magnes. Alloys 9 (2021) 1797–1805, doi:10.1016/j.jma.2020.09.001.
[41] Z.R. Zeng, M.Z. Bian, S.W. Xu, C.H. Davies, N. Birbilis, J.F. Nie, Scr Mater. 108 (2015) 6–10, doi:10.1016/j.scriptamat.2015.06.009.
[42] A. Levinson, R.K. Mishra, R.D. Doherty, S.R. Kalidindi, Acta Mater. 61 (2013) 5966–5978, doi:10.1016/j.actamat.2013.06.037.
[43] A.D. Murphy, J.E. Allison, Metall. Mater. Trans. A: Phys. Metall. Mater. Sci. 49 (2018) 1492–1508, doi:10.1007/s11661-018-4494-6.
[44] J. Victoria-Hernández, S. Yi, D. Klaumünzer, D. Letzig, Mater. Sci. Eng.: A 761 (2019) 138054, doi:10.1016/j.msea.2019.138054.
[45] R. Pei, S. Korte-Kerzel, T. Al-Samman, J. Mater. Sci. Technol. 50 (2020) 257–270, doi:10.1016/j.jmst.2020.01.014.
[46] F.Z. Mouhib, F. Sheng, R. Mandia, R. Pei, S. Korte-Kerzel, T. Al-Samman, Met. (Basel) 11 (2021) 171, doi:10.3390/met11010171.
[47] V. Venkatesh, Z. Croft, K. Thornton, A. Shahani, Acta Mater. 306 (2026) 121885, doi:10.1016/j.actamat.2025.121885.
[48] D. Montiel, P. Staublin, S. Chakraborty, T. Berman, C. Patil, M. Pilipchuk, V. Sundararaghavan, J. Allison, K. Thornton, Comput. Mater. Sci. 272 (2026) 114869, doi:10.1016/j.commatsci.2026.114869.
[49] F.J. Humphreys, M. Hatherly, Recrystallization and Related Annealing Phenomena, 2nd Edition, Elsevier, Amsterdam; Boston, 2004.